catalysts

MDPI

Article

Design and Optimization of Critical-Raw-Material-Free Electrodes towards the Performance Enhancement of Microbial Fuel Cells

Khair Un Nisa , Williane da Silva Freitas *, Alessandra D'Epifanio and Barbara Mecheri *

Department of Chemical Science and Technologies, University of Rome Tor Vergata, Via della Ricerca Scientifica, 00133 Rome, Italy; nsikrn01@uniroma2.it (K.U.N.); alessandra.d.epifanio@uniroma2.it (A.D.)
* Correspondence: williane.freitas@uniroma2.it (W.d.S.F.); barbara.mecheri@uniroma2.it (B.M.)

Abstract: Microbial fuel cells (MFCs) are sustainable energy recovery systems because they use organic waste as biofuel. Using critical raw materials (CRMs), like platinum-group metals, at the cathode side threatens MFC technology's sustainability and raises costs. By developing an efficient electrode design for MFC performance enhancement, CRM-based cathodic catalysts should be replaced with CRM-free materials. This work proposes developing and optimizing iron-based air cathodes for enhancing oxygen reduction in MFCs. By subjecting iron phthalocyanine and carbon black pearls to controlled thermal treatments, we obtained Fe-based electrocatalysts combining high surface area (628 m^2 g^{-1}) and catalytic activity for O_2 reduction at near-neutral pH. The electrocatalysts were integrated on carbon cloth and carbon paper to obtain gas diffusion electrodes whose architecture was optimized to maximize MFC performance. Excellent cell performance was achieved with the carbon-paper-based cathode modified with the Fe-based electrocatalysts (maximum power density-PD_{max} = 1028 mWm^{-2}) compared to a traditional electrode design based on carbon cloth (619 mWm^{-2}), indicating the optimized cathodes as promising electrodes for energy recovery in an MFC application.

Keywords: waste-to-energy; biofuel cells; air electrodes; oxygen reduction; electrocatalysts

check for updates

Citation: Nisa, K.U.; da Silva Freitas, W.; D'Epifanio, A.; Mecheri, B. Design and Optimization of Critical-Raw-Material-Free Electrodes towards the Performance Enhancement of Microbial Fuel Cells. *Catalysts* **2024**, *14*, 385. https://doi.org/10.3390/catal14060385

Academic Editor: Jin-Song Hu

Received: 18 May 2024
Revised: 6 June 2024
Accepted: 7 June 2024
Published: 15 June 2024

1. Introduction

Global development heavily depends on conventional energy sources derived from fossil fuels. However, the growing use of these sources raises concerns about a potential energy and environmental crisis. Therefore, there is an increasing interest in developing sustainable technologies for energy conversion and storage [1–6]. As the research in bioelectrochemical technologies progresses, integrating microbial fuel cells (MFCs) into an energy transition framework could significantly contribute to a more sustainable future [7–10]. An MFC converts biochemical energy into electrical energy through the metabolism of exoelectrogen microorganisms [11–15]. They operate in near-neutral pH as galvanic cells fed with wastewater, allowing the harvesting of electrical energy from removing organics in waste [16–20]. Despite recent practical implementations of MFCs, the low power density output remains challenging for making their application more widespread [8,19–23].

MFC comprises an anode, cathode, and electrolyte compartment [24]. Organic waste in wastewater undergoes oxidation by exoelectrogen microorganisms colonizing the anode [25–27], among which *Shewanella oneidensis*, *Pseudomonas aeruginosa*, and *Geobacter sulfurreducens* are the exoelectrogens explored for the anodic reaction [28–30]. At the same time, the electron acceptor is reduced at the cathode; the most used electron acceptor is oxygen due to its accessible availability and redox features [31]. The oxygen reduction reaction (ORR) is a pH-dependent reaction, and the low availability of H^+/OH^- in neutral pH electrolytes significantly affects ORR kinetics and, consequently, the MFC performance. A common strategy to accelerate ORR kinetics involves using electrocatalysts at the cathode [32].

According to the literature, three leading families of MFC electrocatalysts can be identified: (i) platinum-group metals (PGMs) [33–35], (ii) metal-free carbon-based materials [36], and (iii) PGM-free catalysts [33,37–39]. While PGM-based catalysts have been conventionally used in MFCs due to their high activity, they are not applicable in MFCs because of their low abundance, high cost, and low-performance durability due to deactivation of the catalytic sites in the MFC environment [40]. Electrocatalysts based on the heteroatom doping (usually B, N, O, S, and P) of carbonaceous materials have been reported as a cost-effective alternative [41]. However, metal-free active sites cannot efficiently convert O_2 through a four-electron pathway, requiring high overpotential and yielding high peroxide intermediate concentrations known to degrade the active sites [42]. Extensive research has focused on developing transition-metal-based (TM-based) ORR electrocatalysts for a multiplicity of fuel cell applications, and catalysts based on metal, nitrogen, and carbon (M-N-C) exhibit remarkable activity toward ORR in a wide pH range [43,44].

Several approaches involving different families of precursors have been reported to develop M-N-C catalysts, including the use of pyrroles, corroles, and porphyrins [45]; N-containing organic molecules [46]; metal-organic frameworks [47,48]; and polymers [49,50]. The strategies for obtaining the M-N_x-C active sites from such precursors can be divided into two categories: molecular catalysts involving room- or low-temperature synthesis steps (wet impregnation, mechanical mixing, ball milling, etc.) [51] and TM single-atom catalysts obtained via high-temperature pyrolysis of the TM-based and nitrogen-rich precursors [52,53]. Molecular catalysts, having pre-formed M-N_4-C active sites, have shown high ORR activity at neutral pH [54–56]; however, they lack stability under varying pH conditions. High-temperature pyrolysis was demonstrated to be crucial for obtaining stable M-N_x-C sites [57–59]. Fe-based catalysts show superior performance compared to catalysts based on Mn, Ni, and Co when integrated into the catalytic layer of MFC cathodes. [60,61]. Despite progress in developing M-N-C catalysts with high activity, their cost and stability remain challenging for their application in MFCs [62–64].

Besides the required features for suitable PGM-free catalysts in an MFC application, the air cathode design is another concern that plays a pivotal role in MFC performance [65]. Air cathodes were found to adapt to the MFC's scale and application, with variations for lab-scale prototypes, wastewater treatment systems, or portable energy generators [4,66]. Their architecture's optimization is central to enhancing MFC performance and efficiency, since it significantly affects the diffusion of reactive species and their related products, activity, stability of the catalyst layer, electron transfer, and water management at the electrode–electrolyte interface [67]. Moreover, long-term stability is essential, necessitating materials that resist microbial fouling, the presence of contaminants from the organic waste, and corrosion [68–71].

The use of Fe-phthalocyanines (FePc) as a precursor for iron and nitrogen has been reported as an efficient approach for obtaining highly active Fe-N_x-C sites after high-temperature pyrolysis steps, highlighting the FePc-derived Fe-N-C materials as a standard catalyst for ORR at a wide pH range [54,58,72,73]. Since the use of cost-effective and stable catalysts at the cathode side of MFC is required for their implementation in the energy scenario, we have adopted a facile synthesis approach based on the pyrolysis of FePc and carbon black pearls for obtaining Fe-N-C O.R.R. catalysts. In this work, we have focused on the design of the air electrode, which can boost the performance of a single-chamber MFC by using critical-raw-material-free catalysts. Combining a stainless-steel mesh-based current collector with a porous carbon-based electrode substrate and an optimized catalyst layer (CL), gas diffusion layer (GDL), and preparation effectively improved MFC performance in terms of power output and durability under operating conditions compared to a traditional electrode design taken as the control. This study highlights the optimized electrode design as a promising CRM-free air cathode for membraneless MFCs.

2. Results and Discussion

The electrocatalysts were synthesized by impregnating carbon black pearls (BPs) with Fe-phthalocyanine followed by pyrolysis in Ar or NH_3 flows at 900 °C for 1 h, as described in the Supplementary Materials. The prepared catalysts were labeled Fe-N-C_Ar and Fe-N-C_NH_3.

Thermogravimetric analysis of the catalyst precursors (Figure S1) indicated the fragmentation and complete carbonization of the iron phthalocyanine macrocycle [74], which is supported by the absence of the diffraction peaks ($2\theta = 10$–$40°$) of pristine FePc (Figure S2), in the XRD patterns of the pyrolyzed Fe-N-C_Ar and Fe-N-C_NH_3 catalysts (Figure S3). As shown in Figure S3, the structure of the catalysts is a combination of carbonaceous material, as indicated by the (002) and (101) planes at $2\theta = 25°$ and $2\theta = 43°$, respectively [75], with iron-based phases. Pyrolysis under an argon atmosphere promoted the formation of iron carbide (Fe_3C, JCPDS reference pattern: 00-003-0989), with a slight contribution of iron oxide (magnetite phase—$FeOFe_2O_3$, JCPDS reference pattern: 96-900-5815), and pyrolysis under ammonia led to the formation of $FeOFe_2O_3$. Oxides can be related to the saturation of in situ formed N_x-C moieties due to an iron content higher than 0.5 wt.% [62,76].

The N_2 adsorption–desorption curves for both catalysts exhibited an IV-type isotherm with a notable H4 hysteresis loop [77] (Figure 1a). The specific surface area (SSA), determined using the BET theory, and the maximum pore volume were 628.42 $m^2\ g^{-1}$ and 0.56 $cm^3\ g^{-1}$ for Fe-N-C_NH_3, 588.27 $m^2\ g^{-1}$ and 0.44 $cm^3\ g^{-1}$ for Fe-N-C_Ar. The beneficial effect of NH_3 as a pyrolysis atmosphere in forming pores and increasing the surface area is also evident in the BJH pore size distribution (Figure 1b). The pore volume distribution is relatively higher for both samples, which have a 1.8 to 19.5 nm pore size. Interestingly, a higher mesopore volume distribution was observed for Fe-N-C_NH_3 (Figure 1b), indicating that pyrolysis under NH_3 is also beneficial for promoting the formation of mesopores, which facilitate reactant diffusion into the electrodes [78].

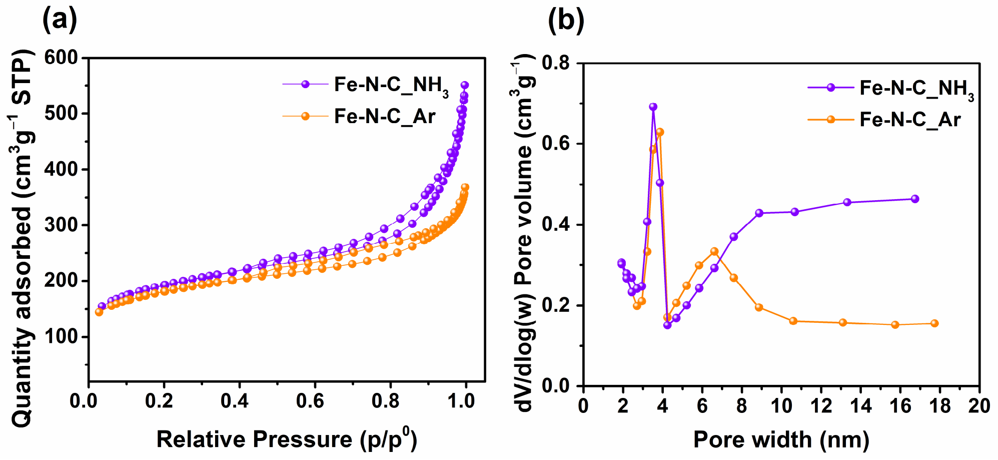

Figure 1. (**a**) N_2 adsorption–desorption isotherms and (**b**) pore size distribution for Fe-N-C_NH_3 and Fe-N-C_Ar catalysts.

2.1. Half-Cell Tests: ORR Activity and Mechanism

Figure 2 shows cyclic voltammograms and RRDE experiments to assess the catalyst's ORR activity and mechanisms when pyrolyzed under Ar or NH_3, Fe-N-C_Ar, and Fe-N-C-NH_3, respectively. The Fe-N-C-NH_3 showed superior catalytic activity performance compared with Fe-N-C_Ar, as evidenced by the more positive potential peak for Fe-N-C_NH_3 in the CV (Figure 2a,b) than Fe-N-C-Ar. The linear sweep voltammetry (Figure 2c) confirms the higher performance of Fe-N-C-NH_3, as indicated by the higher onset potential, half-wave potential, and limiting current for Fe-N-C_NH_3 (0.82 V, 0.66 V and 4.70 mA cm^{-2}) compared with Fe-N-C_Ar (0.80 V, 0.58 V and 4.34 mA cm^{-2}). Additionally, the ring current detected for Fe-N-C-NH_3 was lower than Fe-N-C_Ar (Figure 2d), from which we calculated the electrons transferred *n* (Figure 2e) and H_2O_2 yield % (Figure 2f). For Fe-N-C_NH_3, the peroxide production was lower than 5% and *n* approaches 4, indicating a direct oxygen reduction to water as a reduction pathway during ORR. According to previous studies, the higher ORR activity of the Fe-N-C_NH_3 catalyst can be correlated to the use of NH_3 as a nitrogen secondary source, promoting the content increase in N_x-C active sites and the change in the electronic properties and surface characteristics, combined with the effect of NH_3 on increasing the porosity of the carbon matrix [63,79,80]. The half-cell tests confirm the effectivity of pyrolysis under the NH_3 atmosphere, obtaining a highly active ORR catalyst. Therefore, Fe-N-C_NH_3 was selected for integration in cathodes.

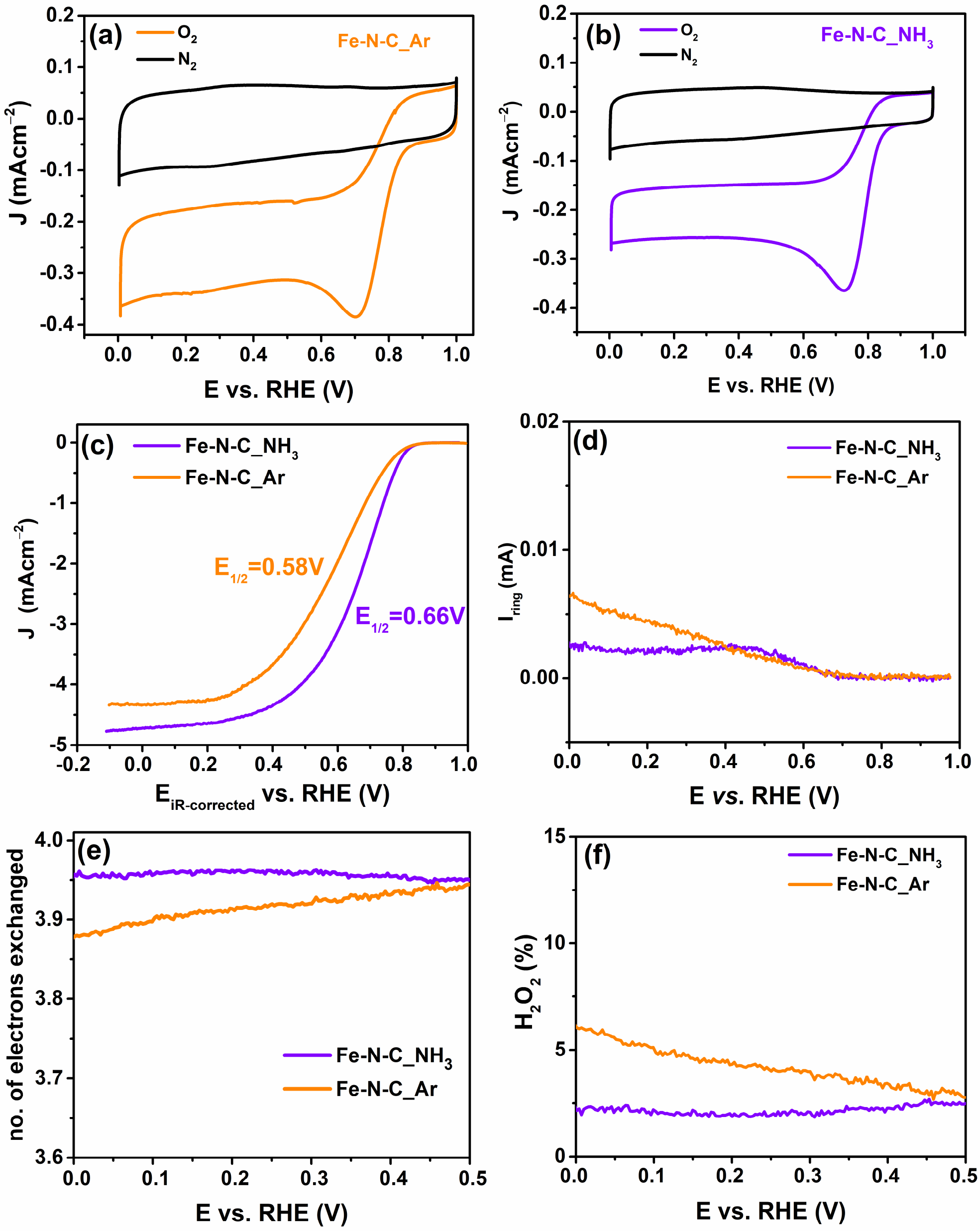

Figure 2. (**a**,**b**) Cyclic voltammetry, (**c**) disk current density, (**d**) ring current, (**e**) number of electrons transferred, and (**f**) hydrogen peroxide percentage for Fe-N-C_Ar and Fe-N-C_NH_3.

2.2. Catalyst Integration into the Air Electrodes and Cell Testing

After optimizing the procedure for obtaining carbon-cloth-based cathodes (CC-cathodes) and carbon-paper-based cathodes (CP-cathodes), Fe-N-C_NH_3 was integrated into CC-cathodes and CP-cathodes as described in Section 3 (Materials and Methods).

The cathode durability was evaluated by monitoring voltage generation cycles over time (90 days), as shown in Figure 3a. The CP-cathode generated more stable cell voltage cycles than the CC-cathode. During the initial 10–20 days, MFCs equipped with CC-cathodes demonstrated a relatively stable voltage response compared to days 30–40, where a drop in cell voltage was observed. The subsequent recovery in cell voltage for the CC-equipped M.F.C. during days 70 to 80 can be ascribed to biofilm stabilization and cathode activation and stabilization processes. Variations in oxygen diffusion rates to the cathode can also contribute to fluctuations, especially in the early stages of operation when inconsistent oxygen availability may occur, potentially influenced by non-optimized cathode architecture.

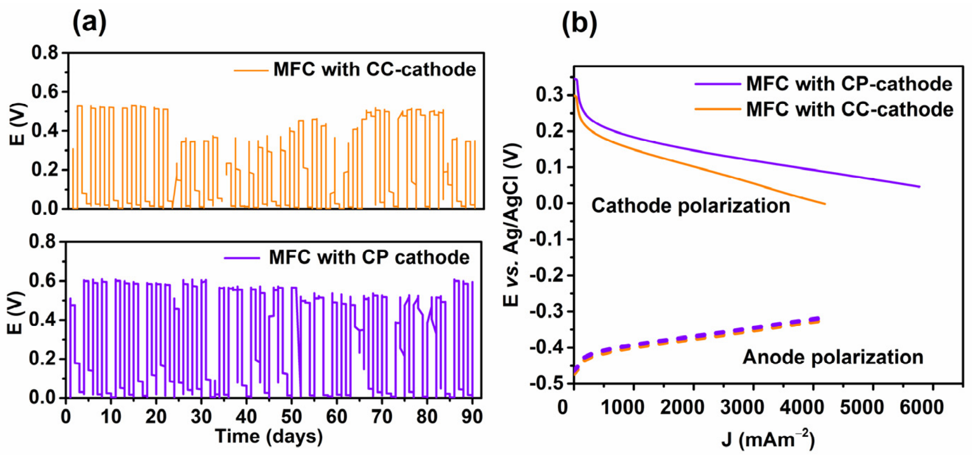

Figure 3. (**a**) Cell voltage generation cycles (under 1 kΩ resistance) over 90 days from the beginning of the experiment and (**b**) separate anode (dotted line) and cathode (solid line) polarization curve for freshly assembled MFCs with the CC-cathode or CP-cathode.

At the beginning of the experiments, the cell voltage obtained for the MFC equipped with the CP-cathode was 0.61 V, reaching 0.52 and 0.58 V after 60 and 90 days, respectively. In contrast, the cell voltage for the CC-cathode was 0.51 (day 0), 0.35 V (day 60), and 0.34 V (day 90), indicating that the CP-cathode's architecture improved the MFC energy output and performance stability.

The cathode and anode polarization curves were separately acquired in a three-electrode configuration using an Ag/AgCl reference electrode (Figure 3b). The anode polarization was similar for all the MFCs investigated, indicating that the main difference in the overall MFC performance was caused by the cathode behavior as enhanced by the cathode polarization. The cathode polarization curves exhibited a linear trend, indicating that the MFCs were predominantly influenced by ohmic behavior, corroborating previous studies reported in the literature [81–83]. The MFC equipped with the CP-cathode consistently outperformed the CC-cathodes in terms of open-circuit voltage, activation overpotential, ohmic overpotential, and mass transport limitation.

EIS spectra were recorded for the freshly assembled (day 0) and aged (after 90 days) CC-cathode and the CP-cathode to investigate their electrochemical behavior under operating conditions. The Nyquist plots (Figure 4) were recorded under open-circuit voltage conditions, showing a high-frequency process associated with charge transfer at the cathode and a low-frequency process linked to mass transfer/diffusion [84]. The Nyquist plots were fitted with the equivalent electrical circuit depicted in the inset of Figure 4a–d. The equivalent circuit comprised ohmic resistance (R_s) corresponding to the solution resistance ranging between 5 and 10 Ω, subtracted from each spectrum. The first CPE denotes a constant phase element associated with the double-layer capacitance. R_{ct} corresponds to the charge transfer resistance, and the second CPE can be ascribed to the biofilm growth onto the cathode. The R_d element indicates the mass transfer/diffusion resistance. For the aged CP cathode, CC-cathode (day 0), and aged CC-cathode (Figure 4b–d), the equivalent circuit comprises an additional Warburg diffusion (W) element in series with R_d, which is included to describe the rising diffusion limitations of reactants and products within the cathode structure due to electrode aging. The Warburg element is absent when modeling the EIS spectra of the fresh CP-cathode due to facilitated oxygen diffusion through the electrode. Nyquist plot fittings for the CP-cathode and CC-cathode are presented in Table 1. The R_{ct} and R_d values for the CP-cathode and CC-cathode at day 0 are 0.88 vs. 2.46 Ω and 14.22 vs. 41.80 Ω, respectively, assuring the advantage of the optimized cathode for reducing activation overpotential. As the cathode ages, it may undergo structural changes or degradation, leading to changes in the pathways for mass transport since MFCs often involve the growth of microbial biofilms on the electrode surfaces. Both types of cathodes underwent aging and exhibited an increase in R_{ct} and R_d values at the end of day 90. However, upon comparison, the R_{ct} and R_d values for the aged CP-cathode and CC-cathode are reported as 1.58 vs. 3.8 Ω and 200 vs. 342 Ω, indicating that the CP-cathode outperforms the CC-cathode.

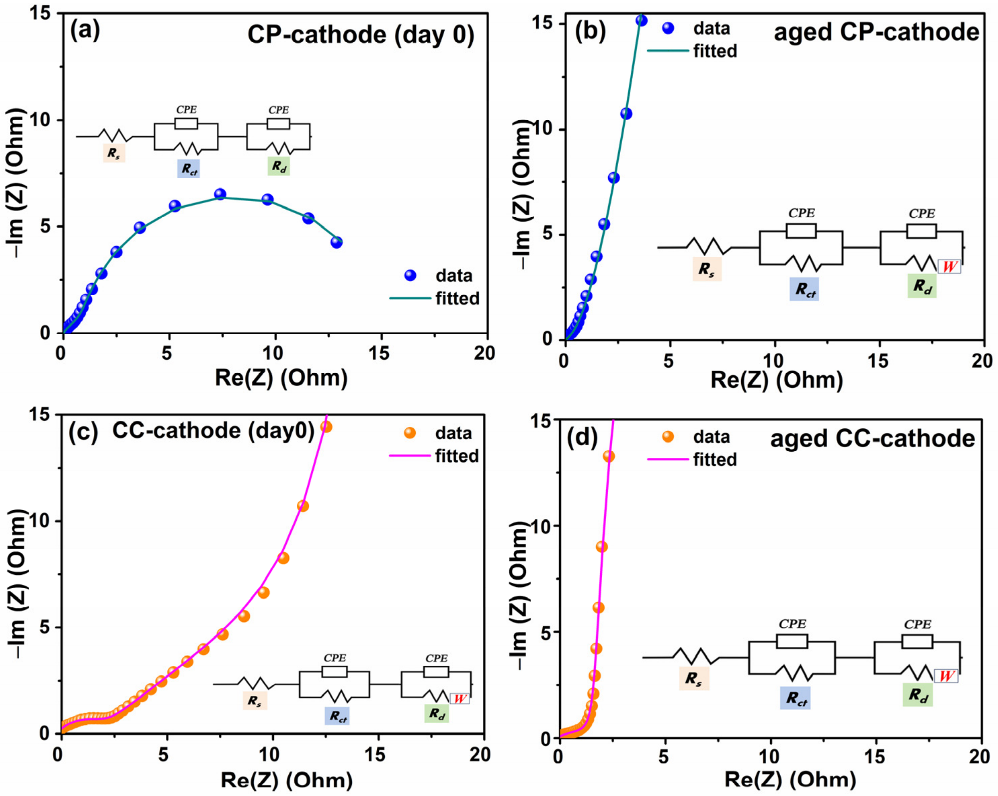

Figure 4. Nyquist plots for freshly assembled (day 0) and aged (day 90) cathodes. (**a**,**b**) CP-cathode and (**c**,**d**) CC-cathodes.

Table 1. Charge and mass transfer resistances of newly assembled vs. aged cathodes.

R_{ct} (Ohm)		R_d (Ohm)	
CP-cathode (day 0) 0.88 ± 0.01	Aged CP-cathode 1.58 ± 0.07	CP-cathode (day 0) 14.22 ± 1.2	Aged CP-cathode 200 ± 3.0
CC-cathode (day 0) 2.46 ± 0.2	Aged CC-cathode 3.80 ± 0.9	CC-cathode (day 0) 41.80 ± 2.0	Aged CC-cathode 342 ± 4.20

Visual, optical, and scanning electron microscopy (SEM) analyses were performed on CC- and CP-cathodes to investigate possible changes in the electrode surface morphology after MFC operation (Figure 5). The cathodes exhibited the formation of a thick biofilm (Figures 5d–h and S4), typically observed for MFC cathodes after long-term operation [70].

Optical microscopy and SEM pictures were taken at the interface between the biofilm and the cathode unexposed area, as illustrated in the red highlighted area in Figure 5d,h.

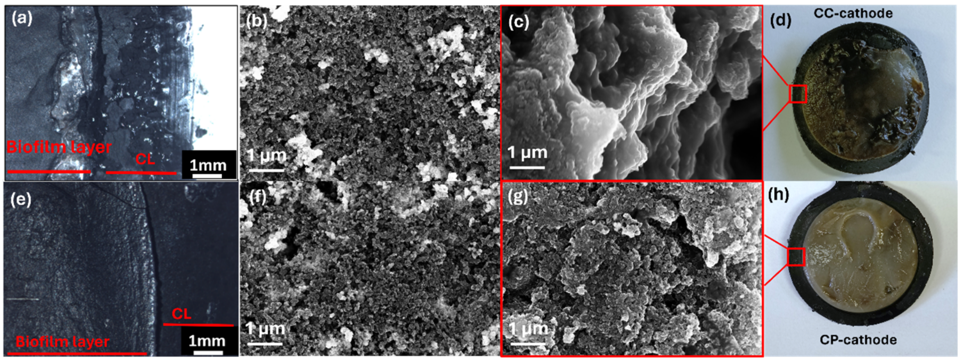

Figure 5. Optical micrographs (**a**,**e**), SEM images (**c**,**g**), and pictures (**d**,**h**) of the CC-cathode (**upper** images) and CP-cathode (**bottom** images) after 90 days of MFC operation. SEM images of fresh (day 0) CC-cathode (**b**) and CP-cathode (**f**).

Optical micrographs revealed a smoother surface for both CP-cathodes as compared to the CC-cathodes. Comparing the biofilm-covered surfaces illustrates that the CP-cathode maintains a more preserved morphology (Figure S5d,e). In contrast, the CC-cathode exhibits more prominent holes (Figure S5a,b). Further comparison of Figure S5c–f underscores the presence of holes in the CC-cathode, suggesting that the integration of the stainless-steel (SS) mesh to the gas diffusion layer (GDL) in the CP-cathode results in more uniform adhesion of the homemade GDL to the electrode, enhancing mechanical stability.

The morphology of the fresh and aged catalyst layers in both electrodes was further investigated by SEM analysis (Figure 5b,c,f,g). SEM micrographs of the fresh CC-cathode (Figure 5b) and CP-cathode (Figure 5f) show that the hot-pressing does not alter the catalyst layer (CL) morphology compared to that of the CC-cathode, showing uniformly distributed carbon-based particles with a porous structure. However, after aging, the catalyst particles on the CC-cathode surface (Figure 5c) appear more aggregated than those on the CP-cathode (Figure 5g).

These findings are consistent with the optical microscopy analysis, showing a more preserved CP-cathode CL morphology. This suggests that the combination of carbon paper as the electrode substrate, SS mesh as the current collector, and the hot-pressing steps effectively maintain the integrity of the electrode CL even after long-term aging.

The curves of potential vs. current and power density recorded for the assembled cells are illustrated in Figure 6 for 0-, 20-, 40-, 60-, and 90-day intervals, and Table 2 shows a comparison between the open-circuit voltage and PD_{max} of the two cathodes and power loss over 90 days.

Table 2. Performance comparison of the MFCs equipped with CP- and CC-cathodes.

Aging Time	**Open-Circuit Voltage (V)**		**PD_{max} (mWm^{-2})**		**Power Loss (%)**	
	CP-cathode	CC-cathode	CP-cathode	CC-cathode	CP-cathode	CC-cathode
Day 0	0.69	0.66	1028	619	-	-
Day 20	0.68	0.65	967	652	5.93	-
Day 40	0.67	0.65	940	646	2.79	1.00
Day 60	0.63	0.64	887	600	5.63	7.12
Day 90	0.63	0.59	616	412	30.5	31.3

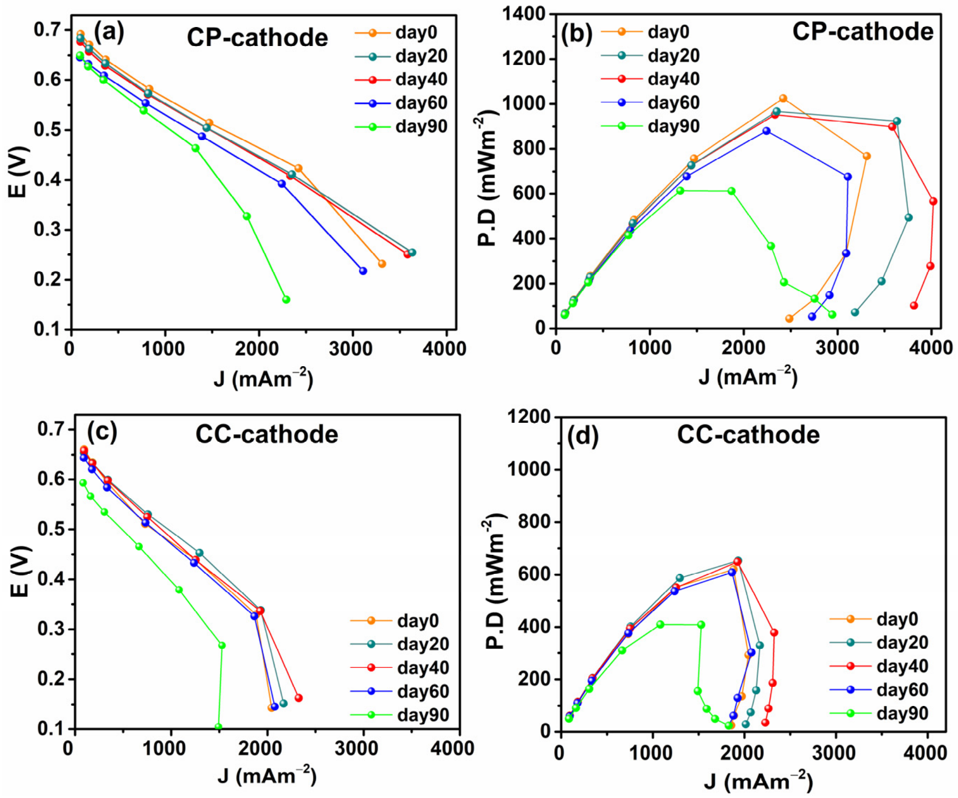

Figure 6. Polarization and power density curves for the MFCs equipped with (**a**,**b**) CP-cathodes and the (**c**,**d**) CC-cathodes over 3 months (0-, 20-, 30-, 40, 60-, and 90-day intervals).

The MFCs assembled with the fresh (day 0) CP-cathode achieved the highest PD$_{max}$ (1028 ± 3 mWm^{-2}), while PD$_{max}$ was 619 ± 2 mWm^{-2} at day 0 for the MFCs equipped with the CC-cathodes. A slight performance fluctuation can be observed for the CC-cathode during the first 40 days, which can be ascribed to cathode activation, also reflected in changes in oxygen diffusion through the electrode [85]. Between day 60 and day 90, both cathodes experienced a drop in power density. The CP-cathode showed a 30.5% PD$_{max}$ drop, and the CC-cathode exhibited a slightly larger PD$_{max}$ drop of 31.3%. At the end of the 90 days, the PD$_{max}$ for the CP-cathode was 616 mWm^{-2}, surpassing the CC-cathode, which had a 412 mWm^{-2} PD$_{max}$. These data highlight the CP-cathode as the best-performing electrode in the single-chamber MFC system. The high performance observed for the CP-cathode arises from the lower thickness and higher porosity of CP compared to that of CC, combined with the optimization of the GDL and catalyst layer preparation, promoting oxygen transport and electron transfer. Additionally, incorporating a stainless-steel-based current collector with an appropriate pore size improved the GDL performance, increasing the power density.

The MFC performance achieved in this work, when compared with that obtained in previously published works for similar cathodes (Table 3), highlights CP-cathodes as potential electrodes for an MFC application since a versatile approach is adopted to obtain catalysts with high ORR activity and air electrodes with competitive performance in the MFC conditions.

Table 3. Performance comparison of MFCs equipped with different PGM-free catalysts based on the literature.

Catalyst	Maximum Power Density (mWm^{-2})	Reference
AC/PTFE	584	[86]
MgO	350	[87]
Fe-N-C	643	[88]
Fe-N-C	1092	[89]
Fe-N-C	699	[90]
TMO	450	[91]
Biochar	528	[92]
Fe-N-C	1200	[93]
Fe-N-C	375	[94]
Fe-N-C_NH_3	1028	This work

3. Materials and Methods

3.1. Electrocatalysts' Synthesis and Air Cathode Assembly

The reagents and materials used in this work are listed in the Supplementary Materials, together with the procedure for preparing activated carbon black pearls (activated BPs).

The Fe-N-C catalysts were prepared by N- and Fe-functionalization of activated BPs, which consisted of dispersing 0.12 g of iron phthalocyanine (FePc) in ethanol (50 mL). Separately, 0.48 g of activated BPs was dispersed in the same volume (50 mL) of solvent. Both suspensions were then sonicated for 15 min. Subsequently, the two suspensions were combined and stirred for 60 min at around 25 °C. The final dispersion was dried (T = 70 °C) for 3 to 4 h. The resulting powder was then ground with the assistance of a mortar and pestle. The samples were then subjected to pyrolysis under either an Ar or NH_3 atmosphere, increasing the temperature at a rate of 20 °C per minute until it reached 900 °C, which was kept for 1 h, obtaining two samples labeled as Fe-N-C_Ar and Fe-N-C_NH_3.

Figure 7 shows the methodology for preparing gas diffusion layer (GDL) cathodes.

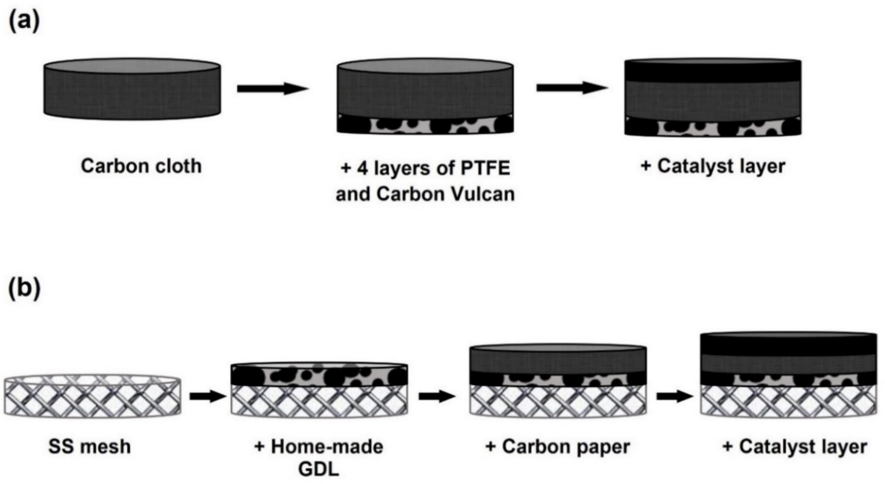

Figure 7. Air cathode preparation schematics. (**a**) Carbon-cloth-based cathodes (CC-cathode) and (**b**) carbon-paper-based cathodes (CP cathode).

CC-cathodes were prepared by applying 4 PTFE-based diffusion layers on the opposite side of the microporous layer (MPL) of ELAT LT1400W MPL carbon cloth (Figure 6a) following established methods [95–97]. A 7 cm^2 electrode was modified by brush painting an ink of Fe-N-C_NH_3 onto the opposite side of the PTFE layers. The catalyst layer comprised 14 mg of the prepared Fe-N-C materials, 47 µL of 2-propanol, 12 µL of deionized water, and 94 µL of 5 wt.% Nafion solution to a total catalyst loading of 2 $mgcm^{-2}$. As previously reported, carbon-paper-based catalysts were prepared by modifying stainless-steel (SS) mesh with a carbon Vulcan/PTFE GDL [98]. Carbon paper was assembled onto the GDL-modified stainless-steel mesh by pressing the surface at 80 °C with a pressure of 4.96 MPa for 1 min (Figure 6b). A catalyst ink based on a suspension of Fe-N-C_NH_3 catalyst into 160 µL of Nafion 5 wt.% and 200 µL of isopropanol solution was then deposited on the CP, maintaining a catalyst loading of 2 $mgcm^{-2}$.

3.2. Methods

Thermogravimetric analysis (TGA) was conducted in a TGA/DSC1 Star System analyzer (Mettler Toledo, Milan, Italy). Mass loss curves were recorded under an N_2 flow, investigated in a temperature range of 25 to 800 °C, at a rate of 5 °C min^{-1}. A Philips PW1730 diffractometer (Cu Kα radiation, λ = 1.5406 A) was used to investigate the phase composition of the precursors and pyrolyzed catalysts. BET SA analysis was carried out by using a Micromeritics® TriStar II Plus (Norcross, GA, USA) surface area and porosity analyzer. The specific surface area (p/p^0 = 0.05–0.3) of the samples was estimated by applying the BET theory, while the pore size distribution was estimated from the Barrett–Joyner–Halenda (BJH) model, applied to the N_2-desorption curve. Before measurements, samples underwent a pretreatment consisting of drying (T = 270 °C) over 12 h in a vacuum system (BUCHI Glass Oven B-585, Milan, Italy) and 1 h under N_2 flow at 300 °C.

The surface morphology of the catalyst layer and GDL of the air cathodes were investigated by optical microscopy using a Nikon SMZ-U, Norcross, GA, USA (zoom 1:10) optical microscope equipped with a Visicam 10.0 photo-camera after an extensive aging period of 11 months in operating microbial fuel cells (MFCs). Before the micrograph acquisition, the electrodes were dried at 50 °C for 1 h. The catalyst layer morphology of the dried electrodes was investigated by scanning electron microscopy using an FE-SEM, Leo Supra 35, Carl Zeiss, Oberkochen, Germany scanning electron microscope.

The electrochemical tests in a standard cell were carried out using a rotating ring disk working electrode (RRDE-AFE6R2GCPT, Pine Research Instrumentation, Durham, NC, USA), a graphite rod counter electrode, and a saturated silver/silver chloride electrode (Ag/AgCl 3.3 M) as the reference electrode. Data recording was carried out using a potentiostat model VMP3 (Bio-Logic Science Instruments, Seyssinet-Pariset, France) under the control of EC-LabV10.18 software. The potential scale vs. the adopted reference electrode was subsequently converted to the reversible hydrogen electrode (RHE), which normalizes the potential values to the pH effect. A 100 mM phosphate-buffered solution (PBS, pH = 7.4) was used as the electrolyte. Before the catalyst ink deposition, the working electrode was first polished with alumina suspension (0.3 µm) and finally polished with a 0.05 µm suspension in a micro-cloth pad (Pine polishing kit, Durham, NC, USA). Then, the glassy carbon disk/platinum ring surface was rinsed and ultrasonicated for 5 min with distilled water. Catalyst inks were prepared by dispersing a proper amount of catalyst in a solution containing isopropanol (425 µL) and Nafion (0.5 wt.% in H_2O, 75 µL) to obtain 0.20 $mgcm^{-2}$ catalyst loading after drop-casting 5 µL of the ink onto the glassy carbon disk (geometric area = 0.196 cm^2). The dispersion was prepared by ultrasonication for 2 h at around 15 °C. The ink layer on the glassy carbon was dried in an oven (T = 40 °C, time = 5 min). Before electrochemical testing, the PBS electrolyte was purged with N_2 for at least 20 min and the surface of the modified WE was activated through cyclic voltammetry (CV) between 0.3 and 1.2 V vs. RHE at 500 mV s^{-1} potential scan rate over 200 CV cycles. Both CV and linear sweep voltammetry (LSV) were adopted to record capacitive and ORR currents after purging the electrolyte with N_2 or O_2. LSV at the disk and the chronoamperometry at the ring (LSV-CA) performed with the RRDE setup during ORR were conducted at a 5 mV s^{-1} scan rate and hydrodynamic conditions (ω = 1600 rpm), scanning the potential between 1.0 and 0.0 V vs. RHE. The Pt-ring was polarized at 1.2 V vs. RHE to record ring current during ORR. The CVs under static conditions were acquired at the same scan rate and potential window. Capacitive current contributions on both disk and ring currents during the ORR were corrected by subtracting the current measured after saturation of the electrolyte with N_2. The reported potentials for the ohmic drop were also corrected by measuring the cell resistance.

The number of electrons transferred (*n*) and the yielding percentage of hydrogen peroxide (H_2O_2%) were calculated as described in the Supplementary Materials and reported in previous papers [47].

MFC tests were conducted in a membraneless reactor (28 mL volume, 4 cm length). The cathode is a 7 cm^2 disk of either the CC-cathode or CP-cathode and the anode consists of a graphite fiber brush, moved from running MFCs, precolonized with the inoculum of wastewaters from Ortona (Zona Industriale Tamarete-Chieti, Italy). The cell was fed with a phosphate-buffered solution (100 mM, pH = 7.4) composed of NH_4Cl (0.62 g L^{-1}), KCl (0.26 g L^{-1}), and CH_3COONa (0.75 g L^{-1}). The MFC tests were conducted in batch mode [99] at room temperature and included two independent replicates for each measurement. The solution was removed from the reactors and replaced by a fresh one whenever the measured voltage (R = 1 kΩ) fell below 40 mV, marking the completion of one operational cycle. The cells were considered acclimated when the voltage output was similar for three consecutive cycles (0.4 V ± 0.05).

Polarization curves were recorded using either a multichannel VSP potentiostat/galvanostat (BioLogic, France) controlled by EC-Lab software in a three-electrode configuration (with Ag/AgCl reference electrode) or a multimeter (2700, Keithley, Cleveland, OH, USA) connected to a personal computer in a two-electrode configuration. In the three-electrode configuration, the cathode and anode polarization curves were separately recorded at a scan rate of 5 mV s^{-1} and the current density was normalized to the cathode geometric area. Electrochemical impedance spectra of cathodes were carried out between 10 mHz and 10 kHz, with an alternating current amplitude of 10 mV. In the two-electrode configuration, polarization curves were obtained by changing a series of external resistances (from 10 to 10 KΩ) on the circuit connected to each cell and measuring the cell voltage every 30 min for each different resistance.

4. Conclusions

This study adopted a facile synthesis approach to develop iron–nitrogen–carbon catalysts derived from iron phthalocyanine, a single source of Fe and N, which were incorporated into a modified carbon-based support. The precursors were subjected to a controlled thermal treatment to promote Fe-N_x-C catalytic site formation as oxygen-reducing centers. The optimization of the pyrolysis conditions under an ammonia flow allows obtaining an electrocatalyst with a high specific surface area (628.42 m^2 g^{-1}) and a high oxygen reduction activity in terms of half-wave potential (0.66 V vs. RHE) and limiting current density (4.70 mA cm^{-2}), with the transferred electrons close to 4, indicating a direct 4e- pathway of oxygen reduction to water.

The Fe-N-C_NH_3 catalyst was integrated at the cathode side of a single-chamber MFC, using either carbon paper (CP-cathode) or carbon cloth (CC-cathode) as catalyst layer substrates. As indicated by the open-circuit voltage, peak power density, and voltage generation cycles, CP-cathodes outperformed CC-cathodes. Electrochemical impedance spectroscopy analysis of the MFC cathode during operation evidenced lower charge transfer and diffusion resistance values for CP-cathodes than CC-cathodes, indicating that optimized electrode design promoted reactive species transport and electron transfer into the cathode. This higher performance is correlated with the thickness and porosity differences between CP and CC, combined with using the stainless-steel mesh current collector and the hot-pressing of the catalyst layer. The use of such components and the optimization of the procedure for their assembly contributed to the integration of the catalyst and the improvement of the energy output and performance durability of the MFCs. The optimized electrode also showed an outstanding performance compared to other PGM-free air cathodes assembled in MFCs. The results highlighted the adopted approach for synthesizing the catalysts and the design of the air cathodes as effective in improving the MFCs energy output, indicating the prepared CRM-free electrodes as promising oxygen-reducing cathode candidates for application in bioelectrochemical systems for energy recovery.

Supplementary Materials: The following supporting information can be downloaded at: https://www.mdpi.com/article/10.3390/catal14060385/s1, Figure S1. TGA curves of the catalyst's precursors [74,100–102]; Figure S2. XRPD patterns for bare Fe phthalocyanine and activated carbon black pearls precursors [103,104]; Figure S3. XRD patterns for the pyrolyzed samples. Figure S4. Pictures of the CC-cathode and CP-cathode after 90 days of MFC operation. Figure S5. Optical micrographs of the catalyst layer and GDL for the CC-cathode and CP-cathode at different magnifications after 90 days of MFC operation.

Author Contributions: Conceptualization, W.d.S.F., A.D. and B.M.; Data curation, K.U.N. and W.d.S.F.; Funding acquisition, B.M.; Investigation, K.U.N. and W.d.S.F.; Methodology, W.d.S.F., B.M. and A.D.; Project administration, B.M. and A.D.; Resources, A.D. and B.M.; Supervision, W.d.S.F., A.D. and B.M.; Writing—original draft, K.U.N. and W.d.S.F.; Writing—review and editing, W.d.S.F., B.M. and A.D. All authors have read and agreed to the published version of the manuscript.

Funding: This work received funding from the European Union—Next Generation EU in response to the MUR (Ministry of University and Research) call "PRIN (Project of National Interest) 2022": Project code: 20224WLXRK.

Data Availability Statement: Data used to support the findings of this study are available within the article and its Supplementary Materials.

Conflicts of Interest: The authors declare no conflicts of interest.

References

1. Cao, J.; Shi, Y.; Xin, J.; Kong, S.; Wang, X. Application of Microbial Fuel Cells with Tungsten-Based Semiconductor Modified Electrode in the Treatment of Cr (VI) Pollutions. *Biochem. Eng. J.* **2023**, *198*, 109034. [CrossRef]
2. Gao, J.Y.; Pu, K.B.; Bai, J.R.; Ma, P.C.; Cai, W.F.; Guo, K.; Chen, Q.Y.; Wang, Y.H. Boosted Biodegradation of Recalcitrant Bisphenol S by Mix-Cultured Microbial Fuel Cells under Micro-Aerobic Condition. *Biochem. Eng. J.* **2023**, *197*, 108968. [CrossRef]
3. Kim, K.C.; Lin, X.; Liu, X.; Wang, L.; Li, C. Stimulation of Electron Transfer in Electricigens by MnxCoySz Heterostructure for the Enhanced Power Generation of Microbial Fuel Cell. *Biochem. Eng. J.* **2023**, *200*, 109089. [CrossRef]
4. Roy, H.; Rahman, T.U.; Tasnim, N.; Arju, J.; Rafid, M.M.; Islam, M.R.; Pervez, M.N.; Cai, Y.; Naddeo, V.; Islam, M.S. Microbial Fuel Cell Construction Features and Application for Sustainable Wastewater Treatment. *Membranes* **2023**, *13*, 490. [CrossRef] [PubMed]
5. Galvis E, A.R.; Leardini, F.; Ares, J.R.; Cuevas, F.; Fernandez, J.F. Simulation and Design of a Three-Stage Metal Hydride Hydrogen Compressor Based on Experimental Thermodynamic Data. *Int. J. Hydrogen Energy* **2018**, *43*, 6666–6676. [CrossRef]
6. Jiménez-Arévalo, N.; Leardini, F.; Ferrer, I.J.; Ares, J.R.; Sánchez, C.; Saad Abdelnabi, M.M.; Betti, M.G.; Mariani, C. Ultrathin Transparent B–C–N Layers Grown on Titanium Substrates with Excellent Electrocatalytic Activity for the Oxygen Evolution Reaction. *ACS Appl. Energy Mater.* **2020**, *3*, 1922–1932. [CrossRef]
7. Mecheri, B. Waste-to-Energy: Microbial Fuel Cells as an Innovation Platform for Sustainable Development. In *Encyclopedia of Electrochemistry*; Wiley: Hoboken, NJ, USA, 2021; pp. 1–24.
8. Kamali, M.; Guo, Y.; Aminabhavi, T.M.; Abbassi, R.; Dewil, R.; Appels, L. Pathway towards the Commercialization of Sustainable Microbial Fuel Cell-Based Wastewater Treatment Technologies. *Renew. Sustain. Energy Rev.* **2023**, *173*, 113095. [CrossRef]
9. Meylani, V.; Surahman, E.; Fudholi, A.; Almalki, W.H.; Ilyas, N.; Sayyed, R.Z. Biodiversity in Microbial Fuel Cells: Review of a Promising Technology for Wastewater Treatment. *J. Environ. Chem. Eng.* **2023**, *11*, 109503. [CrossRef]
10. Yaqoob, A.A.; Ibrahim, M.N.M.; Al-Zaqri, N. A Pilot Trial in the Remediation of Pollutants Simultaneously with Bioenergy Generation through Microbial Fuel Cell. *J. Environ. Chem. Eng.* **2023**, *11*, 110643. [CrossRef]
11. Bose, D.; Bhattacharya, R.; Mukherjee, A. Bibliometric Analysis of Research Trends in Microbial Fuel Cells for Wastewater Treatment. *Biochem. Eng. J.* **2024**, *202*, 109155. [CrossRef]
12. Mejía-López, M.; Lastres, O.; Alemán-Ramirez, J.L.; Lobato-Peralta, D.R.; Verde, A.; Gámez, J.J.M.; de Paz, P.L.; Verea, L. Conductive Carbon-Polymer Composite for Bioelectrodes and Electricity Generation in a Sedimentary Microbial Fuel Cell. *Biochem. Eng. J.* **2023**, *193*, 108856. [CrossRef]
13. Cai, J.; Qaisar, M.; Chen, B.; Wang, K.; Wang, R.; Lou, J. Deciphering the Roles of Suspended Sludge and Fixed Sludge at Electrode in Microbial Fuel Cell Accomplishing Sulfide-Based Autotrophic Denitrification. *Biochem. Eng. J.* **2023**, *193*, 108874. [CrossRef]
14. Yuan, J.; Huang, H.; Chatterjee, S.G.; Wang, Z.; Wang, S. Effective Factors for the Performance of a Co-Generation System for Bioethanol and Electricity Production via Microbial Fuel Cell Technology. *Biochem. Eng. J.* **2022**, *178*, 108309. [CrossRef]
15. Logan, B.E.; Hamelers, B.; Rozendal, R.; Schröder, U.; Keller, J.; Freguia, S.; Aelterman, P.; Verstraete, W.; Rabaey, K. Microbial Fuel Cells: Methodology and Technology. *Environ. Sci. Technol.* **2006**, *40*, 5181–5192. [CrossRef] [PubMed]

16. Oliot, M.; Galier, S.; Roux de Balmann, H.; Bergel, A. Ion Transport in Microbial Fuel Cells: Key Roles, Theory and Critical Review. *Appl. Energy* **2016**, *183*, 1682–1704. [CrossRef]
17. Rinaldi, A.; Mecheri, B.; Garavaglia, V.; Licoccia, S.; Di Nardo, P.; Traversa, E. Engineering Materials and Biology to Boost Performance of Microbial Fuel Cells: A Critical Review. *Energy Environ. Sci.* **2008**, *1*, 417–429. [CrossRef]
18. Hassan, M.; Kanwal, S.; Singh, R.S.; Ali SA, M.; Anwar, M.; Zhao, C. Current Challenges and Future Perspectives Associated with Configuration of Microbial Fuel Cell for Simultaneous Energy Generation and Wastewater Treatment. *Int. J. Hydrogen Energy* **2023**, *50*, 323–350. [CrossRef]
19. Qiu, S.; Guo, Z.; Naz, F.; Yang, Z.; Yu, C. An Overview in the Development of Cathode Materials for the Improvement in Power Generation of Microbial Fuel Cells. *Bioelectrochemistry* **2021**, *141*, 107834. [CrossRef]
20. Borja-Maldonado, F.; López Zavala, M.Á. Contribution of Configurations, Electrode and Membrane Materials, Electron Transfer Mechanisms, and Cost of Components on the Current and Future Development of Microbial Fuel Cells. *Heliyon* **2022**, *8*, e09849. [CrossRef]
21. Prasad, J.; Tripathi, R.K. Review on Improving Microbial Fuel Cell Power Management Systems for Consumer Applications. *Energy Rep.* **2022**, *8*, 10418–10433. [CrossRef]
22. Wang, Z.; Cao, C.; Zheng, Y.; Chen, S.; Zhao, F. Abiotic Oxygen Reduction Reaction Catalysts Used in Microbial Fuel Cells. *ChemElectroChem* **2014**, *1*, 1813–1821. [CrossRef]
23. Lai, B.-L.; Liao, H.-X.; Zhou, S.-Q.; Wei, H.-X.; Li, A.-Y.; Li, N.; Liu, Z.-Q. Chalcogen-Modified Copper-Nitrogen Co-Doped Carbon as a Stable and Efficient Antimicrobial Cathode Catalyst for Microbial Fuel Cells. *J. Environ. Chem. Eng.* **2023**, *11*, 111076. [CrossRef]
24. Wang, H.; Park, J.D.; Ren, Z.J. Practical Energy Harvesting for Microbial Fuel Cells: A Review. *Environ. Sci. Technol.* **2015**, *49*, 3267–3277. [CrossRef] [PubMed]
25. Pan, X.; Wang, W.; Chen, Y.; Wen, Q.; Li, X.; Lin, C.; Wang, J.; Xu, H.; Yang, L. Bio-Electrocatalyst Fe_3O_4/Fe@C Derived from M.O.F. as a High-Performance Bioanode in Single-Chamber Microbial Fuel Cell. *Biochem. Eng. J.* **2022**, *187*, 108611. [CrossRef]
26. Kim, K.Y.; Rossi, R.; Regan, J.M.; Logan, B.E. Enumeration of Exoelectrogens in Microbial Fuel Cell Effluents Fed Acetate or Wastewater Substrates. *Biochem. Eng. J.* **2021**, *165*. [CrossRef]
27. Cheng, P.; Yang, C.; Zhou, S.; Huang, J.; Liu, R.; Yan, B. Degradation Efficiency of Antibiotics by the Sewage-Fed Microbial Fuel Cells Depends on Gram-Staining Property of Exoelectrogens. *Process Saf. Environ. Prot.* **2023**, *176*, 421–429. [CrossRef]
28. Heydorn, R.; Engel, C.; Krull, R.; Dohnt, K. Strategies for the Targeted Improvement of Anodic Electron Transfer in Microbial Fuel Cells. *ChemBioEng Reviews* **2019**, *7*, 4–17. [CrossRef]
29. Li, M.; Zhou, M.; Tian, X.; Tan, C.; McDaniel, C.T.; Hassett, D.J.; Gu, T. Microbial Fuel Cell (M.F.C.) Power Performance Improvement through Enhanced Microbial Electrogenicity. *Biotechnol. Adv.* **2018**, *36*, 1316–1327. [CrossRef] [PubMed]
30. Ma, Y.; Zhang, Z.; Gao, S.; Zhan, Y.; Wei, Z.; Liu, Y. The Efficient Congo Red Decolorization Coupled with Electricity Generation via G. Sulfurreducens Based on Microbial Fuel Cells. *J. Environ. Chem. Eng.* **2023**, *11*, 111296. [CrossRef]
31. Ficca, V.C.A.; Santoro, C.; Marsili, E.; da Silva Freitas, W.; Serov, A.; Atanassov, P.; Mecheri, B. Sensing Nitrite by Iron-Nitrogen-Carbon Oxygen Reduction Electrocatalyst. *Electrochim. Acta* **2022**, *402*, 139514. [CrossRef]
32. Yang, J.; Tian, J.; Zhao, Y.; Wu, Y.; Zhang, Y.; Zhao, K.; Li, S.; Wang, R.; Yang, Y.; Chen, J.; et al. Improving the Bioelectrochemical Performance of Microbial Fuel Cells Using Single-Atom Catalyst Nickel Combined with Graphitic Carbon Nitride as the Cathode Catalyst. *Int. J. Hydrogen Energy* **2024**, *50*, 1257–1266. [CrossRef]
33. Antolini, E. Composite Materials for Polymer Electrolyte Membrane Microbial Fuel Cells. *Biosens. Bioelectron.* **2015**, *69*, 54–70. [CrossRef] [PubMed]
34. Yuan, H.; Hou, Y.; Abu-Reesh, I.M.; Chen, J.; He, Z. Oxygen Reduction Reaction Catalysts Used in Microbial Fuel Cells for Energy-Efficient Wastewater Treatment: A Review. *Mater. Horizons* **2016**, *3*, 382–401. [CrossRef]
35. Dai, Y.; Di, S.; Guo, Y.; Wang, F.; Wang, Z.; Zhu, H. Carbon Layers Derived from Zeolitic Imidazolate Framework Crystal Shells as a Protective Layer for Pt-Based Catalysts: Boosting Oxygen Reduction Catalytic Activity in Fuel Cells. *Int. J. Hydrogen Energy* **2024**, *57*, 1457–1465. [CrossRef]
36. Zheng, S.; Chen, R.; Yang, J.; Guo, J.; An, W.; Tang, J. Biomass-Derived Nitrogen-Doped Carbons Activated by Zinc Halides for Electrocatalytic Oxygen Reduction Reaction. *Int. J. Hydrogen Energy* **2024**, *58*, 333–340. [CrossRef]
37. Costa de Oliveira, M.A.; Mecheri, B.; D'Epifanio, A.; Zurlo, F.; Licoccia, S. Optimization of PGM-Free Cathodes for Oxygen Reduction in Microbial Fuel Cells. *Electrochim. Acta* **2020**, *334*, 135650. [CrossRef]
38. Iannaci, A.; Pepè Sciarria, T.; Mecheri, B.; Adani, F.; Licoccia, S.; D'Epifanio, A. Power Generation Using a Low-Cost Sulfated Zirconium Oxide Based Cathode in Single Chamber Microbial Fuel Cells. *J. Alloys Compd.* **2017**, *693*, 170–176. [CrossRef]
39. Lei, G.; Wu, J.; Qin, L.; Wu, S.; Zhang, F.; Fan, X.; Peng, W.; Li, Y. Graphene Hydrogel Bridged Pyrolysis Strategy: Carbon Cladded Fe2N Nanoparticles in Graphene Matrix for Efficient Oxygen Reduction Reaction. *Int. J. Hydrogen Energy* **2024**, *58*, 1088–1097. [CrossRef]
40. Trapero, J.R.; Horcajada, L.; Linares, J.J.; Lobato, J. Is Microbial Fuel Cell Technology Ready? An Economic Answer towards Industrial Commercialization. *Appl. Energy* **2017**, *185*, 698–707. [CrossRef]
41. Rangraz, Y.; Heravi, M.M. Recent Advances in Metal-Free Heteroatom-Doped Carbon Heterogonous Catalysts. *RSC Adv.* **2021**, *11*, 23725–23778. [CrossRef]

42. Ghasemi, M.; Shahgaldi, S.; Ismail, M.; Kim, B.H.; Yaakob, Z.; Daud, W.R.W. Activated Carbon Nanofibers as an Alternative Cathode Catalyst to Platinum in a Two-Chamber Microbial Fuel Cell. *Int. J. Hydrogen Energy* **2011**, *36*, 13746–13752. [CrossRef]
43. Huang, Y.; Chen, Y.; Xu, M.; Asset, T.; Tieu, P.; Gili, A.; Kulkarni, D.; De Andrade, V.; De Carlo, F.; Barnard, H.S.; et al. Catalysts by Pyrolysis: Direct Observation of Chemical and Morphological Transformations Leading to Transition Metal-Nitrogen-Carbon Materials. *Mater. Today* **2021**, *47*, 53–68. [CrossRef]
44. Dong, F.; Wu, M.; Chen, Z.; Liu, X.; Zhang, G.; Qiao, J.; Sun, S. Atomically Dispersed Transition Metal-Nitrogen-Carbon Bifunctional Oxygen Electrocatalysts for Zinc-Air Batteries: Recent Advances and Future Perspectives. *Nanomicro Lett.* **2022**, *14*, 36. [CrossRef]
45. Zhang, W.; Lai, W.; Cao, R. Energy-Related Small Molecule Activation Reactions: Oxygen Reduction and Hydrogen and Oxygen Evolution Reactions Catalyzed by Porphyrin- and Corrole-Based Systems. *Chem. Rev.* **2017**, *117*, 3717–3797. [CrossRef] [PubMed]
46. Wu, B.; Meng, H.; Morales, D.M.; Zeng, F.; Zhu, J.; Wang, B.; Risch, M.; Xu, Z.J.; Petit, T. Nitrogen-Rich Carbonaceous Materials for Advanced Oxygen Electrocatalysis: Synthesis, Characterization, and Activity of Nitrogen Sites. *Adv. Funct. Mater.* **2022**, *32*, 2204137. [CrossRef]
47. Da Silva Freitas, W.; D'Epifanio, A.; Lo Vecchio, C.; Gatto, I.; Baglio, V.; Ficca, V.C.A.; Placidi, E.; Mecheri, B. Tailoring M.O.F. Structure via Iron Decoration to Enhance O.R.R. in Alkaline Polymer Electrolyte Membrane Fuel Cells. *Chem. Eng. J.* **2023**, *465*, 142987. [CrossRef]
48. Kumar, R.; Mooste, M.; Ahmed, Z.; Zekker, I.; Käärik, M.; Marandi, M.; Leis, J.; Kikas, A.; Otsus, M.; Treshchalov, A.; et al. Catalyzing Oxygen Reduction by Morphologically Engineered ZIF-Derived Carbon Composite Catalysts in Dual-Chamber Microbial Fuel Cells. *J. Environ. Chem. Eng.* **2024**, *12*, 112242. [CrossRef]
49. Yin, X.; Chung, H.T.; Martinez, U.; Lin, L.; Artyushkova, K.; Zelenay, P. PGM-Free O.R.R. Catalysts Designed by Templating PANI-Type Polymers Containing Functional Groups with High Affinity to Iron. *J. Electrochem. Soc.* **2019**, *166*, F3240. [CrossRef]
50. Ricciardi, B.; Mecheri, B.; da Silva Freitas, W.; Ficca, V.C.A.; Placidi, E.; Gatto, I.; Carbone, A.; Capasso, A.; D'Epifanio, A. Porous Iron-Nitrogen-Carbon Electrocatalysts for Anion Exchange Membrane Fuel Cells (AEMFC). *ChemElectroChem* **2023**, *10*, e202201115. [CrossRef]
51. Osmieri, L. Transition Metal–Nitrogen–Carbon (M–N–C) Catalysts for Oxygen Reduction Reaction. Insights on Synthesis and Performance in Polymer Electrolyte Fuel Cells. *ChemEngineering* **2019**, *3*, 16. [CrossRef]
52. Santoro, C.; Serov, A.; Gokhale, R.; Rojas-Carbonell, S.; Stariha, L.; Gordon, J.; Artyushkova, K.; Atanassov, P. A Family of Fe-N-C Oxygen Reduction Electrocatalysts for Microbial Fuel Cell (MFC.) Application: Relationships between Surface Chemistry and Performances. *Appl. Catal. B* **2017**, *205*, 24–33. [CrossRef]
53. Shao, M.; Chang, Q.; Dodelet, J.P.; Chenitz, R. Recent Advances in Electrocatalysts for Oxygen Reduction Reaction. *Chem. Rev.* **2016**, *116*, 3594–3657. [CrossRef] [PubMed]
54. Mecheri, B.; Gokhale, R.; Santoro, C.; Oliveira, M.; D'Epifanio, A.; Licoccia, S.; Serov, A.; Artyushkova, K.; Atanassov, P. Oxygen Reduction Reaction Electrocatalysts Derived from Iron Salt and Benzimidazole and Aminobenzimidazole Precursors and Their Application in Microbial Fuel Cell Cathodes. *ACS Appl. Energy Mater.* **2018**, *1*, 5755–5765. [CrossRef] [PubMed]
55. Santoro, C.; Serov, A.; Stariha, L.; Kodali, M.; Gordon, J.; Babanova, S.; Bretschger, O.; Artyushkova, K.; Atanassov, P. Iron Based Catalysts from Novel Low-Cost Organic Precursors for Enhanced Oxygen Reduction Reaction in Neutral Media Microbial Fuel Cells. *Energy Environ. Sci.* **2016**, *9*, 2346–2353. [CrossRef]
56. Aysla Costa De Oliveira, M.; D'Epifanio, A.; Ohnuki, H.; Mecheri, B. Platinum Group Metal-Free Catalysts for Oxygen Reduction Reaction: Applications in Microbial Fuel Cells. *Catalysts* **2020**, *10*, 475. [CrossRef]
57. Reddy Samala, N.; Friedman, A.; Elbaz, L.; Grinberg, I. Identification of a Durability Descriptor for Molecular Oxygen Reduction Reaction Catalysts. *J. Phys. Chem. Lett.* **2024**, *15*, 481–489. [CrossRef] [PubMed]
58. Ramaswamy, N.; Tylus, U.; Jia, Q.; Mukerjee, S. Activity Descriptor Identification for Oxygen Reduction on Nonprecious Electrocatalysts: Linking Surface Science to Coordination Chemistry. *J. Am. Chem. Soc.* **2013**, *135*, 15443–15449. [CrossRef] [PubMed]
59. Artyushkova, K.; Serov, A.; Rojas-Carbonell, S.; Atanassov, P. Chemistry of Multitudinous Active Sites for Oxygen Reduction Reaction in Transition Metal–Nitrogen–Carbon Electrocatalysts. *J. Phys. Chem. C* **2015**, *119*, 25917–25928. [CrossRef]
60. Erable, B.; Oliot, M.; Lacroix, R.; Bergel, A.; Serov, A.; Kodali, M.; Santoro, C.; Atanassov, P. Iron-Nicarbazin Derived Platinum Group Metal-Free Electrocatalyst in Scalable-Size Air-Breathing Cathodes for Microbial Fuel Cells. *Electrochim. Acta* **2018**, *277*, 127–135. [CrossRef]
61. Zhang, S.; Zhang, S.; Liu, H.; Li, L.; Guo, R. Fe-N-C-Based Cathode Catalyst Enhances Redox Reaction Performance of Microbial Fuel Cells: Azo Dyes Degradation Accompanied by Electricity Generation. *J. Environ. Chem. Eng.* **2023**, *11*, 109264. [CrossRef]
62. Jaouen, F.; Marcotte, S.; Dodelet, J.-P.; Lindbergh, G. Oxygen Reduction Catalysts for Polymer Electrolyte Fuel Cells from the Pyrolysis of Iron Acetate Adsorbed on Various Carbon Supports. *J. Phys. Chem. B* **2003**, *107*, 1376–1386. [CrossRef]
63. Zitolo, A.; Goellner, V.; Armel, V.; Sougrati, M.T.; Mineva, T.; Stievano, L.; Fonda, E.; Jaouen, F. Identification of Catalytic Sites for Oxygen Reduction in Iron- and Nitrogen-Doped Graphene Materials. *Nat. Mater.* **2015**, *14*, 937–942. [CrossRef] [PubMed]
64. Ficca, V.C.A.; Santoro, C.; Placidi, E.; Arciprete, F.; Serov, A.; Atanassov, P.; Mecheri, B. Exchange Current Density as an Effective Descriptor of Poisoning of Active Sites in Platinum Group Metal-Free Electrocatalysts for Oxygen Reduction Reaction. *ACS Catal.* **2023**, *13*, 2162–2175. [CrossRef]

65. Liu, S.-H.; Lin, W.-H.; Lin, C.-W. Increasing Power Output and Isopropanol Biodegradation by Trickle-Bed Microbial Fuel Cells by Optimizing Air Relative Humidity and Oxygen Flux at Cathode. *J. Environ. Chem. Eng.* **2023**, *11*, 110343. [CrossRef]
66. Tremouli, A.; Pandis, P.K.; Kamperidis, T.; Argirusis, C.; Stathopoulos, V.N.; Lyberatos, G. Performance Comparison of Different Cathode Strategies on Air-Cathode Microbial Fuel Cells: Coal Fly Ash as a Cathode Catalyst. *Water* **2023**, *15*, 862. [CrossRef]
67. Andersen, S.M.; Dhiman, R.; Larsen, M.J.; Skou, E. Importance of Electrode Hot-Pressing Conditions for the Catalyst Performance of Proton Exchange Membrane Fuel Cells. *Appl. Catal. B* **2015**, *172–173*, 82–90. [CrossRef]
68. Majlan, E.H.; Rohendi, D.; Daud, W.R.W.; Husaini, T.; Haque, M.A. Electrode for Proton Exchange Membrane Fuel Cells: A Review. *Renew. Sustain. Energy Rev.* **2018**, *89*, 117–134. [CrossRef]
69. Osmieri, L.; Meyer, Q. Recent Advances in Integrating Platinum Group Metal-Free Catalysts in Proton Exchange Membrane Fuel Cells. *Curr. Opin. Electrochem.* **2022**, *31*, 100847. [CrossRef]
70. Kolajo, O.O.; Pandit, C.; Thapa, B.S.; Pandit, S.; Mathuriya, A.S.; Gupta, P.K.; Jadhav, D.A.; Lahiri, D.; Nag, M.; Upadhye, V.J. Impact of Cathode Biofouling in Microbial Fuel Cells and Mitigation Techniques. *Biocatal. Agric. Biotechnol.* **2022**, *43*, 102408. [CrossRef]
71. Li, D.; Liu, J.; Qu, Y.; Wang, H.; Feng, Y. Analysis of the Effect of Biofouling Distribution on Electricity Output in Microbial Fuel Cells. *RSC Adv.* **2016**, *6*, 27494–27500. [CrossRef]
72. Wu, X.; Cheng, Y.; Veder, J.P.; Jiang, S.P. An Efficient Bio-Inspired Oxygen Reduction Reaction Catalyst: MnOx Nanosheets Incorporated Iron Phthalocyanine Functionalized Graphene. *Energy Environ. Mater.* **2021**, *4*, 474–480. [CrossRef]
73. Ma, Y.; Li, J.; Liao, X.; Luo, W.; Huang, W.; Meng, J.; Chen, Q.; Xi, S.; Yu, R.; Zhao, Y.; et al. Heterostructure Design in Bimetallic Phthalocyanine Boosts Oxygen Reduction Reaction Activity and Durability. *Adv. Funct. Mater.* **2020**, *30*, 1–8. [CrossRef]
74. Wang, Z.; Jia, K.; Liu, X. Effect of Elevated Annealing Temperature on Electrical Conductivity and Magnetic Properties of Iron Phthalocyanine Polymer. *J. Polym. Res.* **2016**, *23*, 48. [CrossRef]
75. Yang, H.; Chen, X.; Chen, W.-T.; Wang, Q.; Cuello, N.C.; Nafady, A.; Al-Enizi, A.M.; Waterhouse, G.I.N.; Goenaga, G.A.; Zawodzinski, T.A.; et al. Tunable Synthesis of Hollow Metal–Nitrogen–Carbon Capsules for Efficient Oxygen Reduction Catalysis in Proton Exchange Membrane Fuel Cells. *ACS Nano* **2019**, *13*, 8087–8098. [CrossRef] [PubMed]
76. Kumar, Y.; Kibena-Põldsepp, E.; Kozlova, J.; Rähn, M.; Treshchalov, A.; Kikas, A.; Kisand, V.; Aruväli, J.; Tamm, A.; Douglin, J.C.; et al. Bifunctional Oxygen Electrocatalysis on Mixed Metal Phthalocyanine-Modified Carbon Nanotubes Prepared via Pyrolysis. *ACS Appl. Mater. Interfaces* **2021**, *13*, 41507–41516. [CrossRef] [PubMed]
77. Sing, K.S.W. Adsorption Methods for the Characterization of Porous Materials. *Adv. Colloid Interface Sci.* **1998**, *76–77*, 3–11. [CrossRef]
78. Xu, H.; Wang, D.; Yang, P.; Du, L.; Lu, X.; Li, R.; Liu, L.; Zhang, J.; An, M. A Hierarchically Porous Fe-N-C Synthesized by Dual Melt-Salt-Mediated Template as Advanced Electrocatalyst for Efficient Oxygen Reduction in Zinc-Air Battery. *Appl. Catal. B* **2022**, *305*, 121040. [CrossRef]
79. Kramm, U.I.; Lefèvre, M.; Larouche, N.; Schmeisser, D.; Dodelet, J.-P. Correlations between Mass Activity and Physicochemical Properties of Fe/N/C Catalysts for the ORR in PEM Fuel Cell via 57Fe Mössbauer Spectroscopy and Other Techniques. *J. Am. Chem. Soc.* **2014**, *136*, 978–985. [CrossRef] [PubMed]
80. da Silva Freitas, W.; D'Epifanio, A.; Ficca, V.C.A.; Placidi, E.; Arciprete, F.; Mecheri, B. Tailoring Active Sites of Iron-Nitrogen-Carbon Catalysts for Oxygen Reduction in Alkaline Environment: Effect of Nitrogen-Based Organic Precursor and Pyrolysis Atmosphere. *Electrochim. Acta* **2021**, *391*, 138899. [CrossRef]
81. Santoro, C.; Kodali, M.; Herrera, S.; Serov, A.; Ieropoulos, I.; Atanassov, P. Power Generation in Microbial Fuel Cells Using Platinum Group Metal-Free Cathode Catalyst: Effect of the Catalyst Loading on Performance and Costs. *J. Power Sources* **2018**, *378*, 169–175. [CrossRef]
82. Kodali, M.; Santoro, C.; Serov, A.; Kabir, S.; Artyushkova, K.; Matanovic, I.; Atanassov, P. Air Breathing Cathodes for Microbial Fuel Cell Using Mn-, Fe-, Co- and Ni-Containing Platinum Group Metal-Free Catalysts. *Electrochim. Acta* **2017**, *231*, 115–124. [CrossRef] [PubMed]
83. Rojas-Carbonell, S.; Artyushkova, K.; Serov, A.; Santoro, C.; Matanovic, I.; Atanassov, P. Effect of PH on the Activity of Platinum Group Metal-Free Catalysts in Oxygen Reduction Reaction. *ACS Catal.* **2018**, *8*, 3041–3053. [CrossRef]
84. Hidalgo, D.; Sacco, A.; Hernández, S.; Tommasi, T. Electrochemical and Impedance Characterization of Microbial Fuel Cells Based on 2D and 3D Anodic Electrodes Working with Seawater Microorganisms under Continuous Operation. *Bioresour. Technol.* **2015**, *195*, 139–146. [CrossRef] [PubMed]
85. Pant, D.; Van Bogaert, G.; Diels, L.; Vanbroekhoven, K. A Review of the Substrates Used in Microbial Fuel Cells (M.F.C.s) for Sustainable Energy Production. *Bioresour. Technol.* **2010**, *101*, 1533–1543. [CrossRef] [PubMed]
86. Dong, H.; Yu, H.; Wang, X.; Zhou, Q.; Feng, J. A Novel Structure of Scalable Air-Cathode without Nafion and Pt by Rolling Activated Carbon and PTFE as Catalyst Layer in Microbial Fuel Cells. *Water Res.* **2012**, *46*, 5777–5787. [CrossRef] [PubMed]
87. Li, M.; Zhou, S.; Xu, M. Graphene Oxide Supported Magnesium Oxide as an Efficient Cathode Catalyst for Power Generation and Wastewater Treatment in Single Chamber Microbial Fuel Cells. *Chem. Eng. J.* **2017**, *328*, 106–116. [CrossRef]
88. Birry, L.; Mehta, P.; Jaouen, F.; Dodelet, J.P.; Guiot, S.R.; Tartakovsky, B. Application of Iron-Based Cathode Catalysts in a Microbial Fuel Cell. *Electrochim. Acta* **2011**, *56*, 1505–1511. [CrossRef]
89. Liu, Y.; Fan, Y.S.; Liu, Z.M. Pyrolysis of Iron Phthalocyanine on Activated Carbon as Highly Efficient Non-Noble Metal Oxygen Reduction Catalyst in Microbial Fuel Cells. *Chem. Eng. J.* **2019**, *361*, 416–427. [CrossRef]

90. Jiang, P.Y.; Xiao, Z.H.; Li, S.H.; Luo, Z.N.; Qiu, R.; Wu, H.; Li, N.; Liu, Z.Q. Sulfuration of Fe–N/C Porous Nanosheets as Bifunctional Catalyst with Remarkable Biocompatibility for High-Efficient Microbial Fuel Cells. *J. Power Sources* **2021**, *512*. [CrossRef]
91. Shahbazi Farahani, F.; Mecheri, B.; Majidi, M.R.; Placidi, E.; D'Epifanio, A. Carbon-Supported Fe/Mn-Based Perovskite-Type Oxides Boost Oxygen Reduction in Bioelectrochemical Systems. *Carbon* **2019**, *145*, 716–724. [CrossRef]
92. Yuan, H.; Deng, L.; Qi, Y.; Kobayashi, N.; Tang, J. Nonactivated and Activated Biochar Derived from Bananas as Alternative Cathode Catalyst in Microbial Fuel Cells. *Sci. World J.* **2014**, *2014*, 832850. [CrossRef] [PubMed]
93. Luo, X.; Han, W.; Du, W.; Huang, Z.; Jiang, Y.; Zhang, Y. Ordered Mesoporous Carbon with Atomically Dispersed Fe-Nx as Oxygen Reduction Reaction Electrocatalyst in Air-Cathode Microbial Fuel Cells. *J. Power Sources* **2020**, *469*, 228184. [CrossRef]
94. Iannaci, A.; Ingle, S.; Domínguez, C.; Longhi, M.; Merdrignac-Conanec, O.; Ababou-Girard, S.; Barrière, F.; Colavita, P.E. Nanoscaffold Effects on the Performance of Air-Cathodes for Microbial Fuel Cells: Sustainable Fe/N-Carbon Electrocatalysts for the Oxygen Reduction Reaction under Neutral PH Conditions. *Bioelectrochemistry* **2021**, *142*, 107937. [CrossRef] [PubMed]
95. Iannaci, A.; Mecheri, B.; D'Epifanio, A.; Lázaro Elorri, M.J.; Licoccia, S. Iron–Nitrogen-Functionalized Carbon as Efficient Oxygen Reduction Reaction Electrocatalyst in Microbial Fuel Cells. *Int. J. Hydrogen Energy* **2016**, *41*, 19637–19644. [CrossRef]
96. Kodali, M.; Gokhale, R.; Santoro, C.; Serov, A.; Artyushkova, K.; Atanassov, P. High Performance Platinum Group Metal-Free Cathode Catalysts for Microbial Fuel Cell (MFC). *J. Electrochem. Soc.* **2017**, *164*, H3041–H3046. [CrossRef]
97. Nguyen, M.T.; Mecheri, B.; D'Epifanio, A.; Pepé Sciarria, T.; Adani, F.; Licoccia, S. Iron Chelates as Low-Cost and Effective Electrocatalyst for Oxygen Reduction Reaction in Microbial Fuel Cells. *Int. J. Hydrogen Energy* **2014**, *39*, 6462–6469. [CrossRef]
98. Nisa, K.U.; da Silva Freitas, W.; Montero, J.; D'Epifanio, A.; Mecheri, B. Development and Optimization of Air-Electrodes for Rechargeable Zn–Air Batteries. *Catalysts* **2023**, *13*, 1319. [CrossRef]
99. Mecheri, B.; Iannaci, A.; D'Epifanio, A.; Auri, A.; Licoccia, S. Carbon-Supported Zirconium Oxide as a Cathode for Microbial Fuel Cell Applications. *ChemPlusChem* **2016**, *81*, 80–85. [CrossRef]
100. Costa de Oliveira, M.A.; Mecheri, B.; D'Epifanio, A.; Placidi, E.; Arciprete, F.; Valentini, F.; Perandini, A.; Valentini, V.; Licoccia, S. Graphene oxide nanoplatforms to enhance catalytic performance of iron phthalocyanine for oxygen reduction reaction in bioelectrochemical systems. *J. Power Sources* **2017**, *356*, 381–388. [CrossRef]
101. Milev, A.S.; Tran, N.; Kannangara, G.S.K.; Wilson, M.A.; Avramov, I. Polymorphic transformation of iron-phthalocyanine and the effect on carbon nanotube synthesis. *J. Phys. Chem. C.* **2008**, *112*, 5339–5347. [CrossRef]
102. Yu, X.; Lai, S.; Xin, S.; Chen, S.; Zhang, X.; She, X.; Zhan, T.; Zhao, X.; Yang, D. Coupling of iron phthalocyanine at carbon defect site via π-π stacking for enhanced oxygen reduction reaction. *Appl. Catal. B Environ.* **2021**, *280*, 119437. [CrossRef]
103. Hof, D.D.; Dinsmore, J.A.; Barber, S.; Suhr, R.; Sco, T.R. Scofield, Structural properties and UV to NIR absorption spectra of metal-free phthalocyanine (H2Pc) thin films. *Fiz. A* **2006**, *3*, 147–164.
104. Gambou-Bosca, A.; Bélanger, D. Chemical Mapping and Electrochemical Performance of Manganese Dioxide/Activated Carbon Based Composite Electrode for Asymmetric Electrochemical Capacitor. *J. Electrochem. Soc.* **2015**, *162*, A5115–A5123.